Astrophys Space Sci (2020) 365:167
https://doi.org/10.1007/s10509-020-03880-9

ORIGINAL ARTICLE

In-orbit background simulation study of SVOM/GRM

Jiang He[1,2] · Jian-Chao Sun[1] · Xing Wen[1,2] · Yong-Wei Dong[1] · Juan Zhang[1] · Lu Li[1] · Jiang-Tao Liu[1] · Shuang Liu[3] · Xin Liu[1,2] · Yang Liu[3] · Hao-Li Shi[1] · Bo-Bing Wu[1,2] · Ling-Jun Wang[1] · Rui-Jie Wang[1] · Li Zhang[1] · Shuang-Nan Zhang[1,2] · Wen-Qiao Zhang[3] · Yan-Yan Zhao[3]

Received: 21 July 2020 / Accepted: 10 October 2020

Abstract The Space-based multi-band astronomical Variable Objects Monitor (SVOM) is a Chinese-French satellite dedicated to the observation and study of Gamma-Ray Bursts (GRBs) and other variable sources. Among the four scientific payloads onboard SVOM, the Gamma-Ray Monitor (GRM) is designed to detect GRBs in the 15 keV to 5 MeV energy range. The final performance of GRM can be affected by the space environment background during the flight. In this paper, the authors present the in-orbit background simulation results by using the GEANT4 Monte-Carlo simulation toolkit. Additionally, we studied the Earth occultation effect of the space background due to the anti-solar pointing strategy of SVOM. The total background count rate of each spectrometer of GRM fluctuates between about 840 counts/s and 1341 counts/s, and is dominated by the cosmic X-ray background. Finally, we discuss the emission lines of the background and their potential use for in-orbit calibration of GRM. Our simulation study results can help to understand the impact of the space radiation environment on GRM with the latest geometrical model and can be further compared and updated with the real in-orbit measurement in the future.

Keywords SVOM · GRM · Space environment background · Geant4 Monte-Carlo simulation · Earth occultation · Gamma-Ray Burst

✉ J. He
hejiang@ihep.ac.cn

1 Key Laboratory of Particle Astrophysics, Institute of High Energy Physics, Chinese Academy of Sciences, Beijing 100049, China

2 University of Chinese Academy of Sciences, Beijing 100049, China

3 Innovation Academy for Microsatellites, Chinese Academy of Sciences, Shanghai 201210, China

1 Introduction

Gamma-Ray Bursts (GRBs) are flashes of gamma-rays that appear randomly in the sky and originate at cosmological distances. They were first discovered by the Vela satellites in the late 1960s accidentally (Klebesadel et al. 1973). In order to understand the nature and properties of GRBs, there were many missions designed dedicated to the GRB detection or optimized for such studies by measuring the GRB spectrum, location, flux and polarization in various energy bands. Examples are the CGRO/BATSE (Fishman et al. 1993), BeppoSAX (Boella et al. 1997), HETE-2 (Ricker et al. 2003), RHESSI (Lin et al. 2003), XMM (Jansen et al. 2001), INTEGRAL (Winkler et al. 2003), Swift (Gehrels et al. 2004), Fermi (Meegan et al. 2009), AstroSat (Seetha and Megala 2017), TG-2/POLAR (Zhang et al. 2019; Produit et al. 2018), HXMT (Zhang et al. 2020; Li 2007).

The SVOM mission is a Low Earth Orbit (LEO) satellite whose principal scientific objective is the detection of GRBs and the monitoring of other transient and variable sources. SVOM will be in operation at an altitude of about 630 km and inclination angle of about 30°, and the launch was planned to be around 2021 (Shun-jing et al. 2020). For the LEO satellite, the cosmic X-ray background (CXB), cosmic rays, high-flux protons in the South Atlantic Anomaly (SAA) region, albedo gamma-rays and Earth reflected cosmic gamma-rays constitute the major space radiation environment which will have impact on the performance of the scientific instruments onboard the satellite. Some preliminary performance studies of GRM showed the influence of the sensitive background with its original mass model (Zhao 2012; Xie 2016). However, as the design of the GRM detector has been optimized since its original format, it is worth to perform a thorough analysis of the in-orbit background of GRM with the latest design.

Published online: 19 October 2020

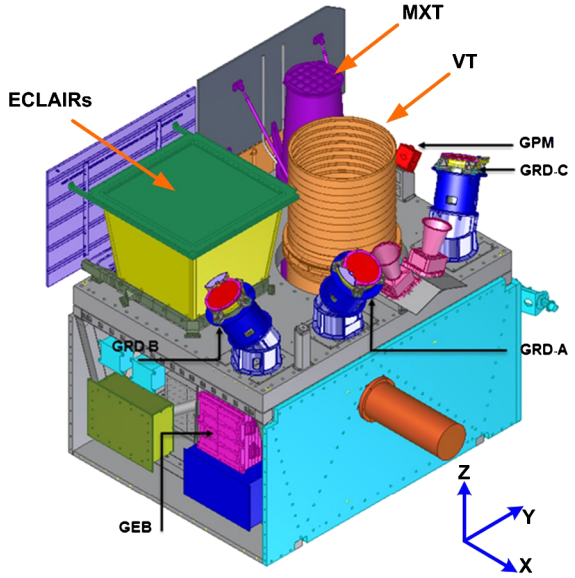

Fig. 1 Mechanical structures of SVOM. The four onboard payloads are shown: ECLAIRs, MXT, VT and GRM. The GRM detector is composed of GRD-A, GRD-B, GRD-C, GPM and GEB

This paper presents the study of the space radiation backgrounds and their influence on the GRM payload onboard SVOM by Monte-Carlo simulation method with the Geant4 toolkit (Agostinelli et al. 2003). With the latest detailed GRM mass model and the simplified mass model of the platform and other surrounding instruments, we estimated the count rate for all the major LEO space radiation backgrounds of GRM and their fluctuations due to the Earth occultation considering the anti-solar pointing operation strategy of SVOM (Cordier et al. 2008). Some possible applications of the background simulation results are also discussed in the last section.

2 The SVOM mission and mass model

The SVOM satellite consists of the platform and four scientific payloads. The four onboard payloads are ECLAIRs (Hard X-ray coded mask imaging camera, 4-120 keV), MXT (Micro-channel X-ray Telescope, 0.2-10 keV), VT (Visible Telescope, 400-950 nm) and GRM (Gamma-Ray Monitor, 15-5000 keV). Besides, there are also ground-based telescopes GWAC (The Ground-based Wide-Angle Camera array) and GFT (The Ground Follow-up Telescope) associated with the SVOM satellite (Wan et al. 2016). All these instruments make it possible for the multi-band and multi-messenger joint detection of GRBs on several aspects, like the real-time trigger and localization, spectrum and flux measurement, etc., for prompt emissions and afterglows. The schematic diagram of the SVOM satellite is shown in Fig. 1.

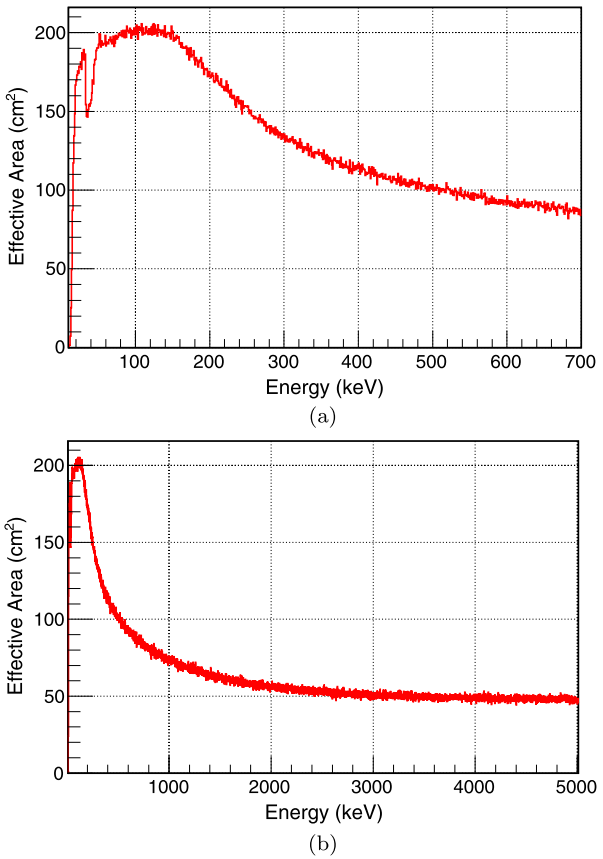

Fig. 2 Simulated effective area of one GRD varies with the photon energy. (**a**) shows the effective area in a narrower energy band of 15 keV to 700 keV with more details. (**b**) shows the effective area in the full detection energy range of 15 keV to 5 MeV

Table 1 The main performance parameters of GRM spectrometer GRD

Performance parameters	Value
Detector crystal	NaI(Tl)
Dimension of the crystal	Diameter: 16 cm
	Thickness: 1.5 cm
Energy detection range	15 keV-5 MeV
Effective area	>200 cm^2 (for one GRD)
Energy resolution	≤16 % @ 60 keV
Time resolution	<20 us

The GRM payload consists of three parts: the three identical spectrometers GRDs (GRD-A, GRD-B and GRD-C), the charged particle monitor GPM and the electronics box GEB, as shown in Fig. 1. The GRDs are the main detectors of GRM, orientating in different directions with an angle of 30 degrees between their observation axis and the z axis, as well as an angle of 120 degrees between each two GRDs in the X-Y axis plane. This design enables GRM to localize GRBs during flight with the different count rate dis-

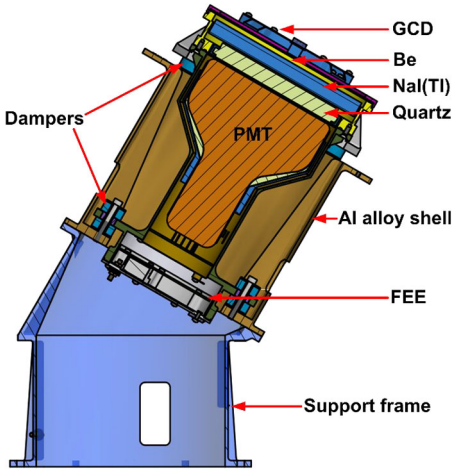

Fig. 3 Schematic diagram of GRD design. The main compositions from top to bottom are GCD, beryllium window, NaI(Tl) scintillator crystal, quartz glass, PMT, FEE and support structure. The aluminum mechanical shell of GRD is 2 mm thick and shields the instruments from low energy photons and charged particles

tributions of the three GRDs. Each GRD is composed of a NaI(Tl) scintillator crystal, photomultiplier tube (PMT), front-end electronics (FEE) and other structural materials. On the top-edge of each GRD there is an in-orbit calibration detector GCD (Wen et al. 2019) that is used for gain calibration during flight. The dimension of the NaI(Tl) crystal is 16 cm in diameter and 1.5 cm in thickness. The schematic diagram of the GRD is shown in Fig. 3. The main performance parameters and effective area of GRD are shown in Table 1 and Fig. 2.

In order to study the performance of GRDs in the space radiation environment, we established a detailed mass model of GRDs and relatively simplified models for the satellite platform, the surrounding instruments and other mechanical structures using the Geant4[1] simulation toolkit. The reason of establishing mass models for the geometrical structures besides GRM is that all those structures may influence the response of GRDs by generating secondary particles which may enter the field of view (FOV) of GRDs. The simplification of those mass models are detailed enough for the study of this work. A constructed mass model of the SVOM satellite with Geant4 toolkit is shown in Fig. 4.

3 The space radiation environment

The main components of radiation background in a NaI(Tl) gamma-ray detector onboard a LEO satellite are the cosmic X-ray background (CXB), albedo gamma-rays and Earth reflected cosmic gamma-rays, cosmic rays (mainly protons, electrons and positrons), as well as delayed background induced by the high energy and flux protons of the SAA region. The albedo neutron results are not included as the contribution of the neutron is negligible compared to other background components according to our simulation results. The spectra and the relevant models of these backgrounds can be acquired from the measurements of other missions (References to specific studies are inserted in the text below.).

[1] http://geant4.web.cern.ch/.

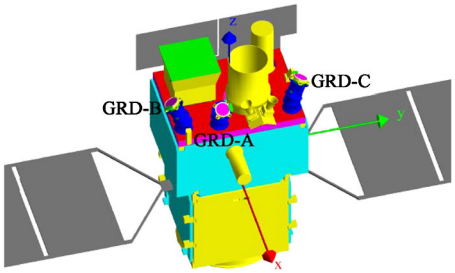

Fig. 4 The SVOM mass model built with Geant4. The platform and major payloads onboard are shown; the solar panels on the two lateral sides are also depicted

3.1 Cosmic X-ray background

The Cosmic X-ray Background (CXB) is generally considered to come from the integrated emission of extragalactic point sources distributed isotropically. The spectrum of CXB can be described as a broken power-law distribution (Gehrels 1992) by the Equation (1):

$$\frac{\mathrm{d}N_{CXB}}{\mathrm{d}E} = \begin{cases} 0.54E^{-1.4} & E < 0.02\ \mathrm{MeV} \\ 0.0117E^{-2.38} & 0.02 \le E < 0.1\ \mathrm{MeV} \\ 0.014E^{-2.3} & E \ge 0.1\ \mathrm{MeV} \end{cases} \quad (1)$$

where the $\mathrm{d}N_{CXB}/\mathrm{d}E$ is in units of counts $\cdot$ cm^{-2} $\cdot$ s^{-1} $\cdot$ MeV^{-1} $\cdot$ sr^{-1}.

3.2 Albedo gamma-rays and reflected gamma-rays

For satellites in low-Earth orbit, the effect of the Earth atmosphere needs to be considered. One radiation source is the albedo gamma photons (Sazonov et al. 2007), which is mainly caused by the interaction between cosmic ray protons and the atmosphere. During the electromagnetic cascade procedure, gamma photons are produced by bremsstrahlung radiation and meson decay. Equation (2) shows the energy spectrum format of the albedo gammas, where the parameter C (counts $\cdot$ cm^{-2} $\cdot$ s^{-1} $\cdot$ sr^{-1}) is related to the geomagnetic dimension, zenith angle, and solar modulation. In first approximation, we assume that the intensity in each direction is the same as in the direction in which the zenith angle is 0 degree. Another radiation source comes from the reflection of CXB by the atmosphere. The spectral model of reflected gamma as described by Equation (3) (Churazov

et al. 2008) is adopted in our study. The reflection coefficient $A(E)$ is described by Equation (4):

$$\frac{\mathrm{d}N_{albedo}}{\mathrm{d}E} = \frac{C}{(E/44)^{-5} + (E/44)^{1.4}} \tag{2}$$

$$\frac{\mathrm{d}N_{reflect}}{\mathrm{d}E} = \frac{\mathrm{d}N_{CXB}}{\mathrm{d}E} \times A(E) \tag{3}$$

$$\begin{aligned} A(E) = & \frac{1.22}{(E/28.5)^{-2.54} + (E/51.3)^{1.57} - 0.37} \\ & \times \frac{2.93 + (E/3.08)^4}{1 + (E/3.08)^4} \\ & \times \frac{0.123 + (E/91.83)^{3.44}}{1 + (E/91.83)^{3.44}} \end{aligned} \tag{4}$$

where the $\mathrm{d}N_{albedo}/\mathrm{d}E$ and $\mathrm{d}N_{reflect}/\mathrm{d}E$ are in units of counts $\cdot$ cm^{-2} $\cdot$ s^{-1} $\cdot$ keV^{-1} $\cdot$ sr^{-1}, and the E in $A(E)$ is in unit of keV.

3.3 Cosmic rays

The major cosmic rays selected for our simulation study are protons, electrons and positrons considering the flux of the cosmic rays and the sensitivity of GRDs. The spectra of the cosmic rays are measured by the AMS experiment (Alcaraz et al. 2000a,b), and the models described by the empirical formulas can be found in (Mizuno et al. 2004).

3.4 SAA delayed background

According to the current orbit operation design, SVOM will pass through the SAA area up to eight times per day, and the average time to pass through the SAA area is about 1200 seconds. GRM will switch off the high voltage (HV) of the GRD PMTs when passing through the SAA region in order to protect the PMT from damage potentially caused by the high flux of trapped protons and electrons. The trapped high energy protons in the SAA region will cause the delayed background. The trapped proton's spectrum (solar minimum) is shown in Fig. 5 which can be acquired from SPENVIS[2] (ESA's Space Environment Information System). In Fig. 5, the high energy segment from 10 MeV to 400 MeV was fitted and the spectrum is described by Equation (5):

$$f(E) = e^{0.042\times(\frac{E}{100})^2 - 0.1\times\frac{E}{10} + 2.32} \tag{5}$$

where the $f(E)$ is in units of counts $\cdot$ cm^{-2} $\cdot$ s^{-1} $\cdot$ MeV^{-1}.

[2] https://www.spenvis.oma.be/.

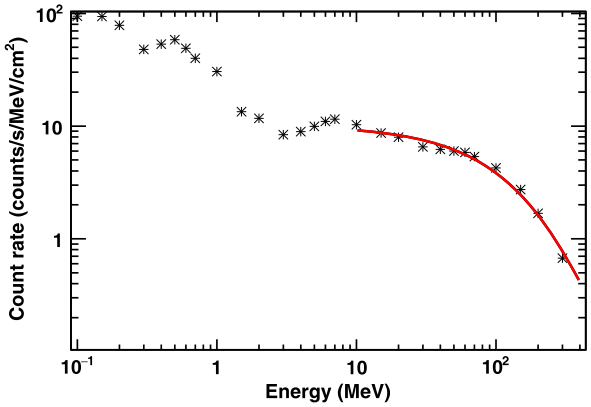

Fig. 5 The spectrum of trapped proton in SAA region got from SPENVIS

4 Simulation process and results

4.1 Simulation process

The Geant4 toolkit is commonly used in the high energy physics and astrophysics for detector performance studies. In our study, the version of Geant4.10.02.p02 was used. Typically, there are three steps before performing the Monte-Carlo simulations. Firstly, the detector mass model should be constructed as detailed as possible, where the materials and geometries should be identical to the real detector. Some simplification of the detectors like the electronics boards and the surrounding payloads and platform are needed to increase the simulation efficiency if they have little or no impact on the final results. Secondly, the physics processes to be simulated have to be chosen and activated within the Geant4 Physics List package. The main physics procedures used in our simulation are standard and low energy electromagnetic process, hadronic process, as well as decay and transportation process. Lastly, the emitters for different sources should be created for various background simulations. Generally, we just need the particle type, energy, time, direction and location as the input parameters for each event simulation run, and we can prepare a set of such input parameters for different purposes. The particle type can be defined at the beginning according to the four kinds of background introduced in Sect. 3. The energy of each particle can be extracted by sampling with the spectrum model.

The spatial distribution of the input particles obeys an isotropic distribution. Figure 6 shows the process of spatial distribution sampling. The emitted particle is generated on the surface of a circle with a radius of r. The distance between the center of the emitter surface and the original point of GRD coordinate is R. Given a direction of the input particle $\overrightarrow{O_1O}$, the position can be generated randomly on the emitter surface.

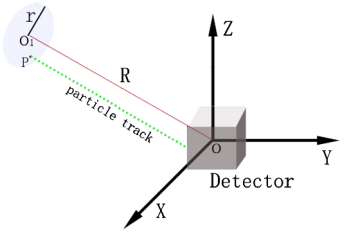

Fig. 6 Location distribution sampling of the input particle. Point P is the position of the input particle. O is the original point in GRD coordinate. The center of the emitter O_1 is evenly distributed within the 4π solid angle FOV of the detector

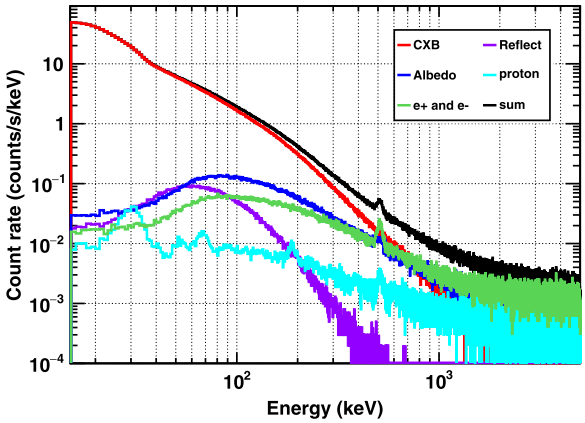

Fig. 7 The simulated background spectra as measured by GRD. The figure shows the case when the Earth is in the −z direction of SVOM

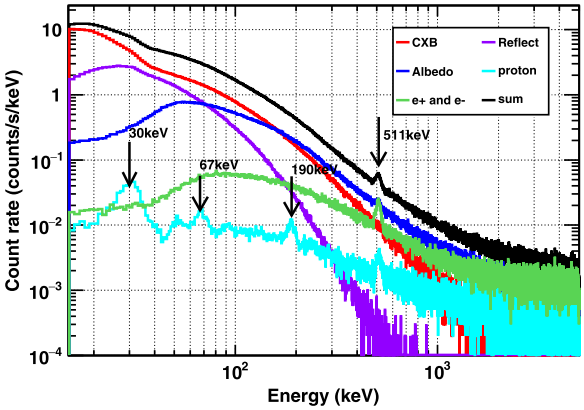

Fig. 8 The simulated background spectra as measured by GRD. The figure shows the case when the Earth is in the z direction of SVOM

Table 2 The simulated count rate (counts/s) of each background component as measured by GRD when the Earth is in the −z direction and +z direction of SVOM respectively

Background	Count rate in −z direction of SVOM	Count rate in +z direction of SVOM
CXB	991.52 ± 0.31	294.43 ± 0.17
Reflected gamma	7.74 ± 0.03	122.87 ± 0.11
Albedo gamma	29.80 ± 0.05	110.41 ± 0.11
Proton	4.79 ± 0.02	5.23 ± 0.02
e– and e+	23.74 ± 0.05	23.74 ± 0.05
SAA	283 ± 1.41	283 ± 1.41
Total	1340.59 ± 1.87	839.68 ± 1.87

4.2 Simulation results

Given a position of the Earth in the GRD coordinate, the input parameters of the particle emitter can be determined with the sampling method described in Sect. 4.1. Here, we have chosen two typical positions for our simulation study: in one the Earth is in the z direction of the satellite which has an angle of 30 degrees relative to the viewing direction of GRD, in the other the Earth is in the –z direction of the satellite which has an angle of 150 degrees relative to the viewing direction of GRD. The CXB, Earth reflected gamma, albedo gamma, cosmic electron and positron are simulated with a timescale of 10000 s, and the cosmic proton is simulated with a timescale of 100 days as its interaction procedure with the detector material is quite long. We choose the particles whose deposited energy is between 15 keV and 5 MeV as the effective events.

The simulated spectra for the considered backgrounds as measured by GRD are shown in Fig. 7 and Fig. 8 after normalization. Our simulated background energy spectrum is similar in magnitude to that of the NaI detectors of Fermi/GBM in 15-1000 keV energy range (Meegan et al. 2009). The delayed background of protons in the SAA region decays rapidly after passing through this area. For simplicity, Table 2 and Fig. 9 only show the average count rate and spectrum of the SAA delayed background in 100 s after SVOM exits the SAA region. Figure 10 shows the SAA count rate changes with time within one day for the different timescales when the GRM is in-orbit for 1 day, 10 days, 50 days and 100 days respectively with the purpose of investigating the delayed background accumulative effect. The results show that after about 50 days, the SAA delayed background (mainly caused by the activation of the Mg element from the aluminum alloy material) is almost stable. It should be noted that the energy resolution measurement result of the GRD has been added in the simulation for the deposited energy of the input particles, which enables the simulation results to better match the measurement results. Table 2 shows the simulated count rate of each background component as measured by GRD when the Earth is in the −z direction and +z direction of SVOM satellite. The error is calculated by $\sqrt{C/t}$, the C is count rate, t is the simulated time. When the energy threshold is 15 keV, the count rates are 1340.59 ± 1.87 counts/s and 839.68 ± 1.87 counts/s respectively. If the threshold is lower, the total background count rate will be higher. It can be concluded that the CXB background component is always dominant in the lower energy part from Fig. 7 and Fig. 8, and also that there are sev-

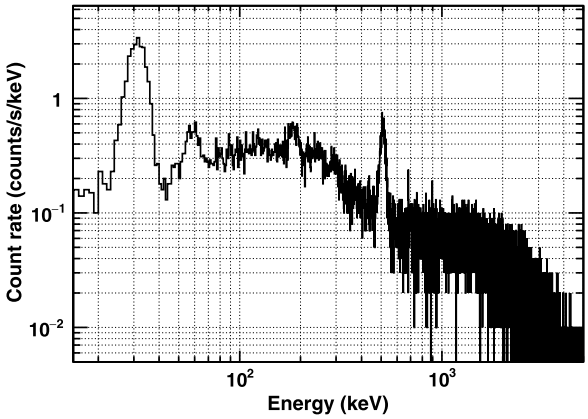

Fig. 9 The simulated average spectrum of the delayed background of the protons as measured by GRD in 100s after the satellite exiting the SAA region

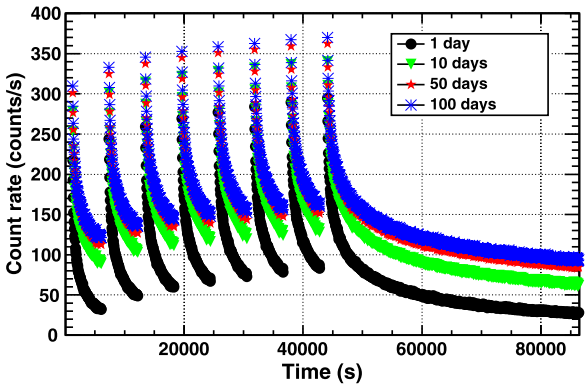

Fig. 10 The SAA delayed background changes with time within one day for four different timescales when the GRM is in orbit for 1 day, 10 days, 50 days and 100 days

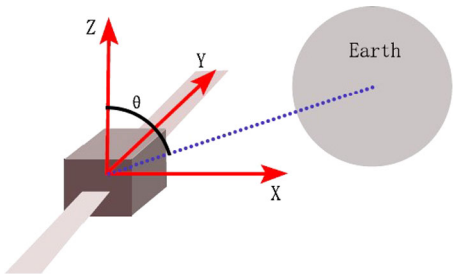

Fig. 11 Illustration of the position of the Earth relative to the SVOM satellite

eral clear emission lines in the background spectra caused by cosmic ray protons and the delayed background of protons in the SAA region. Excluding the SAA delayed background, when the Earth is in the −z and +z directions of SVOM, the CXB accounts for about 90% and 50% of the total background, respectively.

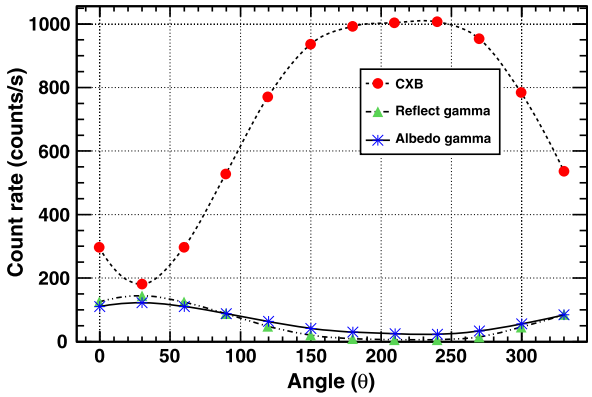

Fig. 12 The gamma-ray background count rates change with the Earth positions in the FOV of SVOM. The x axis in the plot is the angle between the Earth direction and the z axis of SVOM coordinate

4.3 Earth occultation effect

Due to the anti-solar pointing operation strategy of SVOM, the in-flight background components of GRM are modulated by the position of the Earth relative to the z-axis of the satellite. Here for convenience in the study, we assume that the Earth moves around the satellite's y-axis, as shown in Fig. 11. The angle between the direction of Earth position in the SVOM coordinate and the z-axis is θ. It can be inferred that when the Earth is in the viewing direction of GRD, the Earth reflected gamma background should reach the maximum value, while the CXB background will reach its minimum value as detected by GRD. However, when the Earth is behind the GRD, the result is reversed. Figure 12 and Fig. 13 show the change of simulated count rate for different background components as measured by the GRD as a function of the Earth position in θ angle. The figures show that all the background count rates are modulated as function of the Earth's position in the field of view (FOV) of the satellite. The modulation of the proton induced background is opposite to the CXB, which means that the detected protons mostly come from the side or bottom direction of GRD. This is because the protons coming from the side or bottom direction have higher possibility of producing secondary particles which can be detected by GRD through interaction with the shielding shell materials of the GRD detector. However, as the count rate of the cosmic protons is relatively low compared to other backgrounds, it can be omitted. For the albedo gamma-rays and reflected gamma-rays, they have a similar modulation trend as they all come from the Earth atmosphere direction. Table 3 summarizes the simulated count rates as measured by the GRD for four different background components as a function of the position of Earth in the FOV of SVOM.

Table 3 The simulated count rates (counts/s) measured by GRD for each background component when the Earth is in different directions relative to the SVOM z axis

$\theta(^\circ)$	CXB	Reflected gamma	Albedo gamma	Proton	Total
0	294.43 ± 0.17	122.87 ± 0.11	110.41 ± 0.11	5.23 ± 0.02	532.94 ± 0.41
30	179.24 ± 0.13	141.48 ± 0.12	122.45 ± 0.11	5.23 ± 0.02	448.40 ± 0.39
60	293.91 ± 0.17	123.06 ± 0.11	110.60 ± 0.11	5.22 ± 0.02	532.80 ± 0.41
90	527.15 ± 0.23	85.73 ± 0.09	87.73 ± 0.09	5.17 ± 0.02	705.79 ± 0.44
120	768.06 ± 0.28	46.96 ± 0.07	63.76 ± 0.08	5.05 ± 0.02	883.82 ± 0.45
150	936.44 ± 0.31	18.37 ± 0.04	41.11 ± 0.06	4.93 ± 0.02	1000.86 ± 0.44
180	991.52 ± 0.31	7.74 ± 0.03	29.80 ± 0.05	4.79 ± 0.02	1033.85 ± 0.42
210	1002.74 ± 0.32	4.80 ± 0.02	25.07 ± 0.05	4.69 ± 0.02	1037.29 ± 0.41
240	1005.90 ± 0.32	4.04 ± 0.02	22.61 ± 0.05	4.72 ± 0.02	1037.27 ± 0.41
270	952.43 ± 0.31	14.18 ± 0.04	33.49 ± 0.06	4.85 ± 0.02	1004.94 ± 0.43
300	784.00 ± 0.28	42.81 ± 0.07	55.80 ± 0.07	4.97 ± 0.02	887.58 ± 0.44
330	535.10 ± 0.23	83.63 ± 0.09	83.94 ± 0.09	5.14 ± 0.02	707.80 ± 0.44

Note: Table 3 only gives the count rate changes of CXB, Reflect gamma, Albedo gamma and Proton. Here we assume that the positron and electron do not change, because they mainly come from the interaction of the atmosphere with the original cosmic particles, and their distribution is nearly isotropic. The SAA background is only affected by the latitude and longitude of the Earth, and the altitude and inclination angle of SVOM

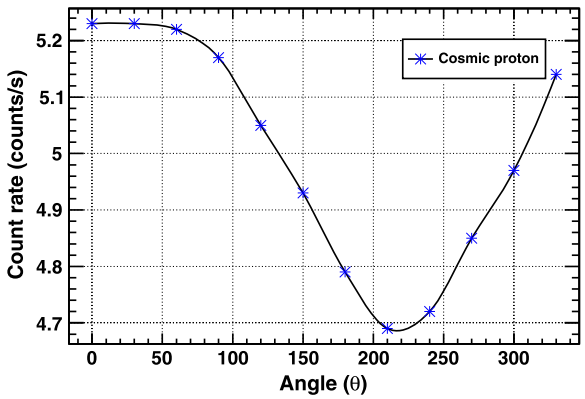

Fig. 13 The simulated proton background count rate changes with the Earth positions in the FOV of SVOM. The x axis in the plot is the angle between the Earth direction and the z axis of SVOM coordinate

5 Summary and discussion

In this work, the different in-orbit backgrounds of GRM and the Earth occultation impact are investigated comprehensively. The GRM mass model has been precisely constructed, along with a simplified geometrical mass model of the platform and other surrounding payloads for Monte-Carlo simulation studies. In our study, we mainly considered the background induced by the CXB, reflected gamma-rays and albedo gamma-rays, cosmic ray and the delayed background after passing through the SAA region. From the Fig. 7 and Fig. 8, we can find that the CXB is the main background for GRM in lower energy range. Excluding the SAA delayed background, the total background count rate is ~ 1057 counts/s when the Earth is in the back of SVOM, and reduces almost half which is ~ 556 counts/s when the Earth is in the FOV center of SVOM. From Fig. 12 and Fig. 13, it can be seen that the change of the CXB induced background with the Earth position is quite obvious, and the trend of the reflected gamma-rays and albedo gamma-rays is opposite to that of the CXB. The change of the proton background with the Earth position is not significant and is opposite to the CXB. They can be approximated as trigonometric function versus the change of angle between the Earth direction and the z axis in SVOM coordinate. Considering that CXB is the main background for GRM, we need to perform more accurate simulations in the future for this component study. The simplified space radiation environment in this study includes only the major backgrounds when the solar cycle is minimum, while the solar activity (solar flare) and geomagnetic field changes are not taken into account. We will study the influence of the solar cycle based on the specific launch time of SVOM in the future. Additionally, the relatively bright X-ray sources such as the Crab (Kirsch et al. 2005), Vela X-1 (Chodil et al. 1967), SwiftJ0243.6+6124 (Kennea et al. 2017), et al. are also not taken into account in our study as they are varying over time. In the next steps, the influence of such sources can be further investigated along with the in-orbit trigger strategy applied in GRM. We can improve the sensitivity of in-orbit triggering and localization accuracy for the measurement of GRBs by GRM in the future based on the work described in this paper.

Additionally, in the future, we need to perform the in-orbit calibration for GRM after launch. The Crab pulsar is both the background and the standard candle for the X-ray measurement instruments, which can be used to perform in-orbit effective area and time precision calibration of the onboard payloads (Kirsch et al. 2005; Li et al. 2020).

The simulated count rate of the Crab is about 90 counts/s in one GRD when the photon is incident perpendicular to the GRD surface. The signal-to-noise ratio of the Crab pulsar is 2.77. The Crab pulsar events can be identified by calculating the time of arrival (TOA) of the events (Li et al. 2019). The GCD detector of GRM contains a ^{241}Am source that can be used for gain calibration of GRD. And the emission line of 0.511 MeV which is caused by the electron-positron annihilation, can also be used for the in-orbit calibration. In addition, we can find some emission lines from the SAA and proton spectra in Fig. 7, Fig. 8 and Fig. 9, which mainly coming from different isotopes of iodine of the NaI(Tl) scintillator. The emission lines from iodine are seen at about 30 keV (various iodine isotopes), 67 keV (^{125}I), and 190 keV (^{123}I). However, these emission lines may be invisible to GRD due to too many CXB events in orbit and relatively low energy resolution of the detector. This will be a topic of a future investigation.

Acknowledgements The authors thank support from the Strategic Priority Research Program of Chinese Academy of Sciences (Grant No. XDA15060303), the National Key Research and Development Program of China (Grant No. 2016YFA0400800), the Joint Research Fund in Astronomy under the cooperative agreement between the National Natural Science Fundation of China and the Chinese Academy of Sciences (Grant No. U1631242), the National Basic Research Program (973 Program) of China (Grant No. 2014CB845800), and the Youth Innovation Promotion Association of Chinese Academy of Sciences (Grant No. 2014009).

References

Agostinelli, S., Allison, J., Amako, K.a., Apostolakis, J., Araujo, H., Arce, P., Asai, M., Axen, D., Banerjee, S., Barrand, G.., et al.: Nucl. Instrum. Methods Phys. Res., Sect. A, Accel. Spectrom. Detect. Assoc. Equip. **506**(3), 250 (2003)

Alcaraz, J., Alpat, B., Ambrosi, G., Anderhub, H., Ao, L., Arefiev, A., Azzarello, P., Babucci, E., Baldini, L., Basile, M., et al.: Phys. Lett. B **484**, 10 (2000a)

Alcaraz, J., Alvisi, D., Alpat, B., Ambrosi, G., Anderhub, H., Ao, L., Arefiev, A., Azzarello, P., Babucci, E., Baldini, L., et al.: Phys. Lett. B **472**, 215 (2000b)

Boella, G., Butler, R.C., Perola, G.C., Piro, L., Scarsi, L., Bleeker, J.A.M.: Astron. Astrophys. Suppl. Ser. **122**(2), 299 (1997)

Chodil, G., Mark, H., Rodrigues, R., Seward, F.D., Swift, C.D.: Astrophys. J. **150**, 57 (1967)

Churazov, E., Sazonov, S., Sunyaev, R., Revnivtsev, M.: Mon. Not. R. Astron. Soc. **385**(2), 719 (2008)

Cordier, B., Desclaux, F., Foliard, J., Schanne, S.: Astrophysics **1000**(1), 585 (2008)

Fishman, G.J., Meegan, C.A., Wilson, R.B., Paciesas, W.S., Pendleton, G.N., Harmon, B.A., Horack, J.M., Brock, M.N., Kouveliotou, C., Finger, M.H.: Astron. Astrophys. Suppl. Ser. **97**(1), 17 (1993)

Gehrels, N.: Nucl. Instrum. Methods Phys. Res. **313**(3), 513 (1992)

Gehrels, N., Chincarini, G., Giommi, P., Mason, K.O., Nousek, J.A., Wells, A., White, N.E., Barthelmy, S.D., Burrows, D.N., Cominsky, L.R., et al.: Astrophys. J. **611**(2), 1005 (2004)

Jansen, F., Lumb, D., Altieri, B., Clavel, J., Ehle, M., Erd, C., Gabriel, C., Guainazzi, M., Gondoin, P., Much, R., et al.: Astron. Astrophys. **365**(1) (2001)

Kennea, J.A., Lien, A.Y., Krimm, H.A., Cenko, S.B., Siegel, M.H.: Astronomers Telegram **10809** (2017)

Kirsch, M., Briel, U., Burrows, D., Campana, S., Cusumano, G., Ebisawa, K., Freyberg, M., Guainazzi, M., Haberl, F., Jahoda, K., et al.: In: UV, X-Ray, and Gamma-Ray Space Instrumentation for Astronomy XIV, vol. 5898, p. 589803 (2005). International Society for Optics and Photonics

Klebesadel, R.W., Strong, I.B., Olson, R.A.: Astrophys. J. **182**, 85 (1973)

Li, T.P.: Nucl. Phys. B, Proc. Suppl. **166**, 131 (2007)

Li, H.-C., Gauvin, N., Ge, M.-Y., Kole, M., Li, Z.-H., Produit, N., Song, L.-M., Sun, J.-C., Szabelski, J., Tymieniecka, T., et al.: J. High Energy Astrophys. **24**, 15 (2019)

Li, X., Li, X., Tan, Y., Yang, Y., Ge, M., Zhang, J., Tuo, Y., Wu, B., Liao, J., Zhang, Y., et al.: J. High Energy Astrophys. **27**, 64 (2020)

Lin, R.P., Dennis, B.R., Hurford, G.J., Smith, D.M., Zehnder, A., Harvey, P.R., Curtis, D.W., Pankow, D., Turin, P., Bester, M., et al.: Sol. Phys. **210**(1), 3 (2003)

Meegan, C.A., Lichti, G.G., Bhat, P.N., Bissaldi, E., Briggs, M.S., Connaughton, V., Diehl, R., Fishman, G.J., Greiner, J., Hoover, A.S., et al.: Astrophys. J. **702**(1), 791 (2009)

Mizuno, T., Kamae, T., Godfrey, G., Handa, T., Thompson, D.J., Lauben, D., Fukazawa, Y., Ozaki, M.: Astrophys. J. **614**(2), 1113 (2004)

Produit, N., Bao, T., Batsch, T., Bernasconi, T., Britvich, I., Cadoux, F., Cernuda, I., Chai, J., Dong, Y., Gauvin, N., et al.: Nucl. Instrum. Methods Phys. Res., Sect. A, Accel. Spectrom. Detect. Assoc. Equip. **877**, 259 (2018)

Ricker, G., Atteia, J.-L., Crew, G., Doty, J., Fenimore, E., Galassi, M., Graziani, C., Hurley, K., Jernigan, J., Kawai, N., et al.: In: AIP Conference Proceedings, vol. 662, p. 3 (2003). American Institute of Physics

Sazonov, S., Churazov, E., Sunyaev, R., Revnivtsev, M.: Mon. Not. R. Astron. Soc. **377**(4), 1726 (2007)

Seetha, S., Megala, S.: Curr. Sci. **113**(04), 579 (2017)

Shun-jing, Y., Francois, G., Jian-yan, W., Shuang-nan, Z., Bertrand, C.: Chin. Astron. Astrophys. **44**(2), 269 (2020)

Wan, M., Wu, C., Wang, J., Qiu, Y., Xin, L., Mullender, S., Muhleisen, H., Scheers, B., Zhang, Y., Nes, N., et al.: Publ. Astron. Soc. Pac. **128**(969), 114501 (2016)

Wen, X., Liu, J., Liu, X., Wang, R., Shi, H., Li, L., Sun, J., Zhang, L., Dong, Y., Wu, B.: At. Energy Sci. Technol. **53**(6), 1091 (2019)

Winkler, C., Courvoisier, T.J.L., Cocco, G.D., Gehrels, N., Gimenez, A., Grebenev, S.A., Hermsen, W., Mashesse, J.M., Lebrun, F., Lund, N., et al.: Astron. Astrophys. **411**(1), 1 (2003)

Xie, F.: Study of the in-flight background for HXMT. PhD thesis, University of Chinese Academy of Sciences (2016)

Zhang, S., Kole, M., Bao, T., Batsch, T., Bernasconi, T., Cadoux, F., Chai, J., Dai, Z., Dong, Y., Gauvin, N., et al.: Nat. Astron. **3**(3), 258 (2019)

Zhang, S., Li, T., Lu, F.J., Song, L., Xu, Y., Liu, C.Z., Chen, Y., Cao, X.L., Bu, Q.C., Cai, C., et al.: Sci. China, Phys. Mech. Astron. **63**(4), 1 (2020)

Zhao, D.-H.: Study of the scientific performances of the high energy payloads on board SVOM. PhD thesis, University of Chinese Academy of Sciences (2012)